Modeling the Diiron Centers of Non-Heme Iron Enzymes. Preparation of Sterically Hindered Diiron(II) Tetracarboxylate Complexes and Their Reactions with Dioxygen

Daniel D. LeCloux, Amy M. Barrios, Tadashi J. Mizoguchi, and Stephen J. Lippard*

Contribution from the Department of Chemistry, Massachusetts Institute of Technology, Cambridge, Massachusetts 02139

Received April 10, 1998

Abstract: A series of diiron(II) complexes, $[Fe_2(\mu\text{-L})(\mu\text{-}O_2CR)(O_2CR)(N)_2]$, where L is a dinucleating bis(carboxylate) ligand based on *m*-xylylenediamine bis(Kemp's triacid imide) and N is a pyridine- or imidazole-derived ligand, were prepared as models for the carboxylate-bridged non-heme diiron cores of the O_2-activating enzymes, soluble methane monooxygenase hydroxylase (MMOH), and the R2 subunit of ribonucleotide reductase (RNR-R2). X-ray crystallographic studies revealed differences in the coordination geometry of the bridging monocarboxylate ligand, which shifts from monodentate to *syn*,*syn*-bidentate bonding modes. The extent of this carboxylate shift depends on both the steric bulk of the monocarboxylate and the basicity of the ancillary N-donor ligands. Exposure of these diiron(II) complexes to O_2 at −77 °C in nonpolar solvents (CH_2Cl_2, THF, toluene) yielded deep blue solutions ($\lambda_{max} \approx 580$ nm, $\epsilon \approx 1200\ M^{-1}\ cm^{-1}$), consistent with the generation of diiron(III) peroxo species. This reaction was irreversible, and its stoichiometry was determined by manometry to be 1:1 in diiron(II) complex and O_2. The diiron(III) peroxo complexes exhibited oxygen isotope-sensitive resonance Raman bands at ∼860 cm^{-1}, which are assigned to the O−O stretching frequency of a μ-1,2-peroxodiiron(III) core. ^{57}Fe Mössbauer spectroscopy confirmed the assignment of the diiron(III) oxidation level and indicated that the two iron sites have inequivalent environments ($\delta_1 \approx 0.47$ mm s^{-1}, $\Delta E_{Q1} \approx 0.88$ mm s^{-1}; $\delta_2 \approx 0.63$ mm s^{-1}, $\Delta E_{Q2} \approx 1.20$ mm s^{-1}). Kinetics experiments provided rate constants for the reaction and revealed it to be first order in both diiron(II) complex and O_2. The factors controlling the rate of formation of the blue species and its stability are discussed.

Introduction

Carboxylate-bridged diiron proteins use dioxygen for functions ranging from O_2 transport to the selective oxidation of organic substrates.[1−5] This functional diversity is illustrated by three of the most intensively studied proteins in this family, hemerythrin, ribonucleotide reductase, and methane monooxygenase. Hemerythrin (Hr) is a dioxygen carrier in certain marine invertebrates. The reduced protein contains a $[Fe_2(\mu\text{-OH})(\mu\text{-}O_2CR)_2(His)_5]^+$ core and binds O_2 in the form of a terminal hydroperoxide ligand that forms a hydrogen bond to the oxo bridge of the resulting (μ-oxo)diiron(III) unit (eq 1). Ribonucleotide reductase from *Escherichia coli* houses a carboxylate-bridged diiron active site in the R2 subunit (RNR-R2), where O_2 is activated such that one of its oxidizing equivalents generates a tyrosyl radical. This radical accepts an electron from the R1 subunit, the site of ribonucleotide reduction. Methane monooxygenase (MMO) is used by obligate methanotrophic bacteria to convert methane selectively to methanol. The soluble form (sMMO) contains a carboxylate-bridged diiron active site in the hydroxylase component (MMOH). This mixed-function oxidase functions such that one of the oxygen atoms from dioxygen is incorporated into methanol and the other into water (eq 2). Figure 1 depicts the active-site structures of the reduced, diiron(II) forms of RNR-R2, and MMOH, as deduced from

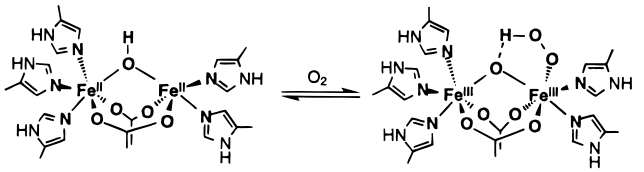

(1)

$$CH_4 + O_2 + NADH + H^+ \rightarrow CH_3OH + H_2O + NAD^+ \quad (2)$$

X-ray crystal structural analyses.[6−8]

A detailed mechanistic picture of O_2 activation in RNR-R2[2,9,10] and sMMO[2,4,9,10] is emerging as a consequence of kinetic and spectroscopic studies which have identified transient intermediates in their reaction cycles. For RNR-R2, the first detectable intermediate forms and decays within 35 ms at 4 °C.[11] On the basis of the similarity of its Mössbauer and UV−vis spectra to those observed for a model complex and an analogous

(1) Feig, A. L.; Lippard, S. J. *Chem. Rev.* **1994**, *94*, 759.
(2) Wallar, B. J.; Lipscomb, J. D. *Chem. Rev.* **1996**, *96*, 2625.
(3) Liu, K. E.; Lippard, S. J. In *Advances in Inorganic Chemistry*; Sykes, A. G., Ed.; Academic Press: San Diego, CA, 1995; Vol. 42, p 263.
(4) Valentine, A. M.; Lippard, S. J. *J. Chem. Soc., Dalton Trans.* **1997**, 3925.
(5) Que, L., Jr. *J. Chem. Soc., Dalton Trans.* **1997**, 3933.
(6) Rosenzweig, A. C.; Brandstetter, H.; Whittington, D. A.; Nordlund, P.; Lippard, S. J.; Frederick, C. A. *Proteins* **1997**, *29*, 141.
(7) Rosenzweig, A. C.; Nordlund, P.; Takahara, P. M.; Frederick, C. A.; Lippard, S. J. *Chem. Biol.* **1995**, *2*, 409.
(8) Nordlund, P.; Eklund, H. *Curr. Opin. Struct. Biol.* **1995**, *5*, 758.
(9) Kurtz, D. M., Jr. *JBIC* **1997**, *2*, 159.
(10) Edmondson, D. E.; Huynh, B. H. *Inorg. Chim. Acta* **1996**, *252*, 399.

S0002-7863(98)01216-5 CCC: $15.00
Published on Web 08/21/1998

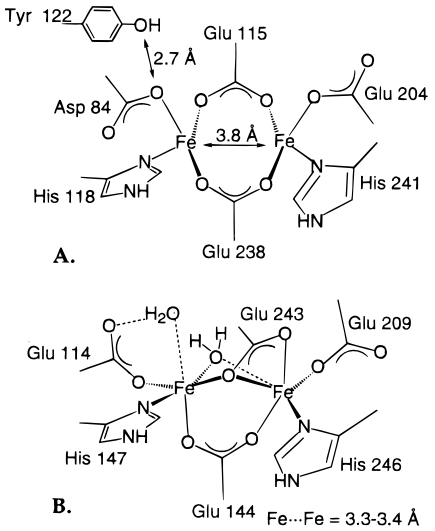

Figure 1. Representations of the active-site structures of (A) reduced RNR-R2 and (B) reduced MMOH (H_{red}).

intermediate in MMOH (vide infra), this species has been tentatively assigned as a diiron(III) peroxo unit. Intermediate X, which evolves subsequently, exhibits Mössbauer,[12] Q-band ENDOR,[13] and EXAFS[14] features consistent with an antiferromagnetically coupled $Fe^{III}Fe^{IV}$ center having at least one oxo bridge and a terminal water or hydroxide ligand. This high-valent intermediate generates the active enzyme formally by hydrogen atom abstraction from Tyr122 to afford an oxo-bridged diiron(III) center and the tyrosyl radical. Intermediate X presumably is the product of O−O bond cleavage, but it is uncertain whether injection of an extra electron must accompany O−O bond scission or whether an as yet unobserved dioxodiiron(IV) species might initially be generated.[10]

For MMOH, a metastable diiron(III) peroxo intermediate (H_{peroxo}) has also been spectroscopically identified as an early product of the O_2 reaction chemistry,[15] but it forms and decays more slowly than its RNR-R2 analogue.[11] H_{peroxo} converts to a diiron(IV) species termed Q.[15,16] This intermediate, or a closely related derivative, is believed to oxidize the substrate, since Q is the last species detected prior to methanol formation and its decomposition is accelerated by the presence of substrates. EXAFS studies of Q revealed parameters quite similar to those of intermediate X in RNR-R2,[17] but the data do not provide unique structural information, particularly with respect to coordination of oxygen ligands derived from O_2.

Considerable effort has been expended to prepare synthetic models for the dioxygen intermediates described above for RNR-R2 and sMMO. The goals have been to mimic their spectroscopy, structural features, and ultimately their oxidation chemistry.[1,5] The most noteworthy systems reported to date include three crystallographically characterized diiron(III) peroxo complexes and a bis(μ-oxo)$Fe^{III}Fe^{IV}$ species, the properties of which are summarized in Table 1.[18−22] The peroxo complexes display relatively intense electronic transitions centered at ~600 nm ($\epsilon \approx 2000\ M^{-1}\ cm^{-1}$) and O−O stretching frequencies at ~900 cm^{-1}. X-ray structural studies revealed the peroxide ligand to be coordinated symmetrically, in either an eclipsed[19,20] or a gauche[18] μ-1,2 bridging mode.

Despite these advances, a model system has yet to be described where a peroxo is derived from the reaction of a diiron(II) precursor with O_2, and which either converts to a high-valent Q- or X-like species or performs hydrocarbon oxidation chemistry. These shortcomings may stem from the fact that the previously reported model systems do not reproduce the ligand composition of the RNR-R2 and sMMO active sites; the relatively soft, nitrogen-rich coordination environments of the model complexes more closely resemble the active site of Hr. The widely different fates of the peroxo species generated in Hr, RNR-R2, and sMMO may be due in part to the ability of the latter two systems, which have harder, more oxygen-rich donor sets, to support the higher iron oxidation states required for O−O bond cleavage. We were therefore interested in investigating more carboxylate-rich synthetic models to determine whether they might more closely mimic the O_2 binding, O−O bond cleavage, and substrate oxidation properties of RNR and sMMO.

In pursuit of this goal, carboxylate-bridged diiron(II) complexes employing the *m*-xylylenediamine bis(Kemp's triacid imide) (H_2XDK) and related ligand systems (**1**−**3**) were

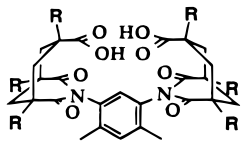

H_2XDK; R = methyl (**1**)
H_2PXDK; R = propyl (**2**)
H_2BXDK; R = benzyl (**3**)

prepared and their reactivity toward dioxygen explored.[23] A family of tris(μ-carboxylato)diiron(II) complexes with a coordination environment analogous to that of the MMOH active site has been obtained. When one such derivative was exposed to O_2 at low temperature in THF, the solution flashed deep purple, but quickly decayed to a red-orange color in less than 15 s (eq 3). Monitoring this reaction by stopped-flow UV−vis

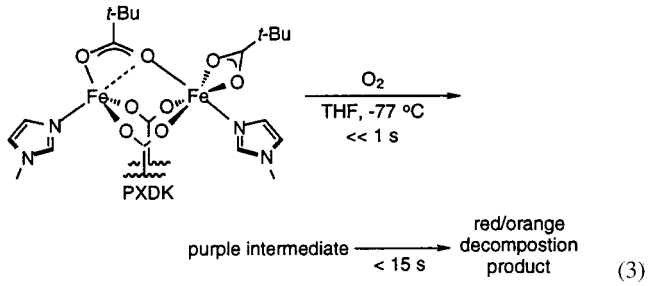

(3)

spectroscopy revealed the buildup and decay over 10 s of an intermediate with an optical band centered at 650 nm. This

(11) Burdi, D.; Riggs-Gelasco, P. J.; Tong, W.; Willems, J.-P.; Lee, H.-I.; Doan, P. E.; Sturgeon, B.; Shu, L.; Chen, S.; Edmonson, D. E.; Huynh, B. H.; Que, L., Jr.; Hoffman, B. M.; Stubbe, J. *Steenbock Symp. Proc.: Biosynthesis and Function of Metal Clusters For Enzymes* **1997**, *25*, 85.
(12) Sturgeon, B. E.; Burdi, D.; Chen, S.; Huynh, B. H.; Edmondson, D. E.; Stubbe, J.; Hoffman, B. M. *J. Am. Chem. Soc.* **1996**, *118*, 7551.
(13) Willems, J.-P.; Lee, H.-I.; Burdi, D.; Doan, P. E.; Stubbe, J.; Hoffman, B. M. *J. Am. Chem. Soc.* **1997**, *119*, 9816.
(14) Riggs-Gelasco, P. J.; Shu, L.; Chen, S.; Burdi, D.; Huynh, B. H.; Que, L., Jr.; Stubbe, J. *J. Am. Chem. Soc.* **1998**, *120*, 849.
(15) Liu, K. E.; Valentine, A. M.; Wang, D.; Huynh, B. H.; Edmondson, D. E.; Salifoglou, A.; Lippard, S. J. *J. Am. Chem. Soc.* **1995**, *117*, 10174.
(16) Lee, S.-K.; Nesheim, J. C.; Lipscomb, J. D. *J. Biol. Chem.* **1993**, *268*, 21569.
(17) Shu, L.; Nesheim, J. C.; Kauffmann, K.; Münck, E.; Lipscomb, J. D.; Que, L., Jr. *Science* **1997**, *275*, 515.
(18) Kim, K.; Lippard, S. J. *J. Am. Chem. Soc.* **1996**, *118*, 4914.
(19) Ookubo, T.; Sugimoto, H.; Nagayama, T.; Masuda, H.; Sato, T.; Tanaka, K.; Maeda, Y.; Okawa, H.; Hayashi, Y.; Uehara, A.; Suzuki, M. *J. Am. Chem. Soc.* **1996**, *118*, 701.
(20) Dong, Y.; Yan, S.; Young, V. G., Jr.; Que, L., Jr. *Angew. Chem., Int. Ed. Engl.* **1996**, *35*, 618.
(21) Dong, Y.; Zang, Y.; Shu, L.; Wilkinson, E. C.; Que, L., Jr.; Kauffmann, K.; Münck, E. *J. Am. Chem. Soc.* **1997**, *119*, 12683.
(22) Que, L., Jr.; Dong, Y. *Acc. Chem. Res.* **1996**, *29*, 190.
(23) Herold, S.; Lippard, S. J. *J. Am. Chem. Soc.* **1997**, *119*, 145.

Table 1. Summary of Data Acquired for Selected RNR-R2 and sMMO Model Complexes

	UV-Vis (λ_{max}, nm (ϵ, M^{-1} cm^{-1}))	Resonance Raman (cm^{-1})		X-Ray (Å)		Mössbauer ($mm\ s^{-1}$)		ref
		ν_{O-O}	ν_{Fe-O}	Fe···Fe	O–O	δ	ΔE_Q	
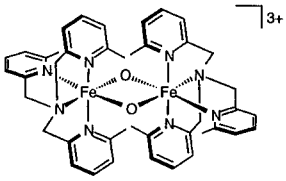	350 (8000)	*a*		*a*		0.48, 0.08	1.6, 0.5	21,22
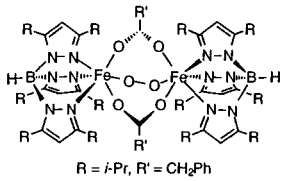 R = *i*-Pr, R' = CH_2Ph	694 (2650)	888	415	4.007(4)	1.406(8)	0.66	1.40	18
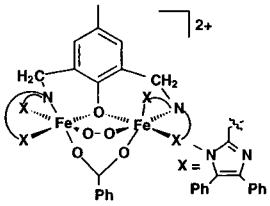	500-800 (1700)	*b*	*b*	3.327(2)	1.426(6)	0.58, 0.65	0.74, 1.70	19
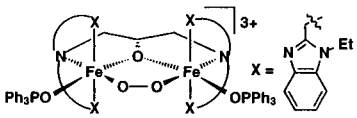	588 (1500)	900	*a*	3.462(2)	1.416(7)	*a*		20

[a] Not reported. [b] Not detected.

chromophore was tentatively assigned to a diiron(III) peroxo species, the inherent instability of which precluded further characterization or functional reactivity studies.

In the present work we have extended this chemistry by synthesizing sterically more hindered ligands with the aim of stabilizing the incipient peroxo intermediate. This strategy was adopted following previous work from our laboratory on the thermal decomposition of well-defined diiron(III) peroxo complexes.[24,25] Kinetic studies revealed the decay to have a second-order dependence on the concentration of the peroxo species, resulting in extrusion of 0.5 equiv of O_2 and cleanly yielding oxo-bridged diiron(III) derivatives. Since bimolecular decay pathways are typically retarded by implementing more sterically demanding ligands, we modified our complexes accordingly. The synthesis and reactivity of these new diiron(II) compounds, their reaction with O_2 to form relatively more stable peroxo adducts, the physical characterization of these species, and studies of the dependence of their rates of formation on the nature of both the N- and O-donor ligands form the basis for the present report. A detailed account of the reactivity of the peroxo complexes toward electrophilic, nucleophilic, and hydrocarbon substrates will be published separately.[26]

Experimental Section

General Considerations. The compounds H_2XDK (**1**),[27] H_2PXDK (**2**),[23] H_2BXDK (**3**),[28] 1-phenylcyclohexanecarboxylic acid (HO_2CPhCy),[29] and [FeTp$^{3,5-iPr_2}$(O_2CCH_2Ph)][18] were prepared according to literature procedures. The thallium(I) salts of the carboxylic acid ligands were obtained as described, or by analogous methods,[28,30] and characterized by ^{1}H NMR spectroscopy. The ligands 1-methylimidazole (Me-Im) and 1-butylimidazole (Bu-Im) were degassed and stored over 3-Å molecular sieves for several days prior to use. Dioxygen (99.994%, BOC Gases) was dried by passing the gas stream through a column of Drierite. All other reagents were procured from commercial sources and used as received unless otherwise noted. Benzene, toluene, pentane, THF, and Et_2O were distilled from sodium benzophenone ketyl under nitrogen. Dichloromethane, 1,2-dichloroethane, and pyridine were distilled from CaH_2 under nitrogen; CD_2Cl_2 was degassed, passed through activated basic alumina, and stored over 3-Å molecular sieves prior to use. All air-sensitive manipulations were carried out either in a nitrogen-filled Vacuum Atmospheres drybox or by standard Schlenk line techniques at room temperature unless otherwise noted.

[Fe(XDK)(py)$_2$] (4). To a rapidly stirred suspension of Tl_2(XDK) (2.00 g, 2.02 mmol) and pyridine (1.64 mL, 20.2 mmol) in THF (15 mL) was added a solution of $FeBr_2$ (446 mg, 2.02 mmol) in THF (5 mL). After 6 h, the precipitated TlBr was removed by filtration through Celite, and the filtrate was evaporated to dryness. The crude residue was washed with pentane (20 mL) to remove any residual pyridine, isolated by filtration, and dried fully in vacuo to afford **4** as a light yellow powder (1.44 g, 90%). This crude material was used for subsequent reactions without further purification. Recrystallization from CH_2Cl_2/pyridine/Et_2O afforded yellow blocks which allowed **4** to be characterized by X-ray crystallography. IR (KBr) 3068, 2961, 2929,

(24) Feig, A. L.; Masschelein, A.; Bakac, A.; Lippard, S. J. *J. Am. Chem. Soc.* **1997**, *119*, 334.
(25) Feig, A. L.; Becker, M.; Schindler, S.; van Eldik, R.; Lippard, S. J. *Inorg. Chem.* **1996**, *35*, 2590.
(26) LeCloux, D. D.; Lippard, S. J. Manuscript in preparation.
(27) Rebek, J., Jr; Marshall, L.; Wolak, R.; Parris, K.; Killoran, M.; Askew, B.; Nemeth, D.; Islam, N. *J. Am. Chem. Soc.* **1985**, *107*, 7476.
(28) LeCloux, D. D.; Lippard, S. J. *Inorg. Chem.* **1997**, *36*, 4035.
(29) Calderon, S. N.; Newman, A. H.; Tortella, F. C. *J. Med. Chem.* **1991**, *34*, 3159.
(30) Doyle, G.; Eriksen, K. A.; Modrick, M.; Ansell, G. *Organometallics* **1982**, *1*, 1613.

1735, 1696, 1602, 1404, 1463, 1358, 1334, 1218, 1195, 1087, 1039, 958, 835, 760, 626 cm^{-1}; UV−vis (CH_2Cl_2) (λ_{max}, nm (ϵ, M^{-1} cm^{-1})) 364 (580). Anal. Calcd for $C_{42}H_{48}N_4O_8Fe$: C, 63.64; H, 6.10; N, 7.07. Found: C, 61.33; H, 6.26; N, 6.60. Since an X-ray structure determination revealed **4** to be the desired material, the disagreement with the expected carbon analysis was not pursued further.

[Fe(BXDK)(py)$_2$] (5). This compound was prepared as a light yellow powder from Tl_2(BXDK) (2.33 g, 1.61 mmol), pyridine (560 μL, 6.92 mmol), and $FeBr_2$ (354 mg, 1.61 mmol) by a procedure analogous to that used to obtain **4** (1.55 g, 77%). The crude material was used for all subsequent reactions. Recrystallization from CH_2Cl_2/Et_2O provided **5** as opaque yellow needles. IR (KBr) 3062, 3027, 2921, 2857, 1734, 1693, 1603, 1495, 1446, 1352, 1191, 1040, 935, 761, 700, 593, 526 cm^{-1}; UV−vis (CH_2Cl_2) (λ_{max}, nm (ϵ, M^{-1} cm^{-1})) 361 (690). Anal. Calcd for $C_{78}H_{72}N_4O_8Fe$: C, 74.99; H, 5.81; N, 4.48. Found: C, 74.45; H, 5.80; N, 4.34.

[Fe$_2$(μ-BXDK)(μ-O$_2$C*t*-Bu)(O$_2$C*t*-Bu)(py)$_2$] (6). To a stirred solution of TlO_2C*t*-Bu (147 mg, 0.480 mmol) and pyridine (116 μL, 1.44 mmol) in THF (3 mL) was added $FeBr_2$ (53 mg, 0.24 mmol) in THF (1 mL). After 10 min this mixture was added in one portion to a stirred solution of **5** (300 mg, 0.240 mmol) in CH_2Cl_2 (3 mL). The resulting mixture was allowed to stir for 0.5 h, after which time the precipitated TlBr was removed by filtration through Celite, and the volatile components were removed in vacuo. Recrystallization from CH_2Cl_2/Et_2O afforded **6** as yellow blocks (265 mg, 73%) which allowed the compound to be characterized by X-ray crystallography. IR (KBr) 3062, 3028, 2959, 2923, 2863, 1734, 1693, 1602, 1541, 1486, 1407, 1365, 1221, 1189, 1042, 937, 763, 701, 608, 528 cm^{-1}; UV−vis (CH_2Cl_2) (λ_{max}, nm (ϵ, M^{-1} cm^{-1})) 355 (920). Anal. Calcd for $C_{88.5}H_{91}N_4O_{12}Fe_2Cl$ (**6**·0.5CH_2Cl_2): C, 68.59; H, 5.92; N, 3.61. Found: C, 68.45; H, 6.06; N, 3.48. One lattice CH_2Cl_2 molecule identified by X-ray crystallography was apparently not removed completely by pumping on the sample in vacuo for 1 d. When this procedure was repeated with heating, the sample decomposed.

[Fe$_2$(μ-XDK)(μ-O$_2$CPhCy)(O$_2$CPhCy)(py)$_2$] (7). This compound was prepared from Tl(O$_2$CPhCy) (308 mg, 0.757 mmol), pyridine (184 μL, 2.27 mmol), $FeBr_2$ (83 mg, 0.378 mmol), and **4** (300 mg, 0.378 mmol), as described for **6**. Recrystallization from benzene/pentane afforded **7** as pale yellow blocks which were characterized by X-ray crystallography (291 mg, 61%). IR (KBr) 3063, 2960, 2928, 2862, 1737, 1699, 1614, 1448, 1405, 1355, 1221, 1187, 1069, 957, 851, 760, 698, 637 cm^{-1}; UV−vis (CH_2Cl_2) (λ_{max}, nm (ϵ, M^{-1} cm^{-1})) 354 (840). Anal. Calcd for $C_{68}H_{78}N_4O_{12}Fe_2$: C, 65.08; H, 6.26; N, 4.46. Found: C, 64.09; H, 6.63; N, 4.08.

[Fe$_2$(μ-XDK)(μ-O$_2$CAr)(O$_2$CAr)(py)$_2$], O$_2$CAr = 2,4,6-Triisopropylbenzoate (8). This compound was prepared from TlO_2CAr (342 mg, 0.757 mmol), pyridine (184 μL, 2.27 mmol), $FeBr_2$ (83 mg, 0.378 mmol), and **4** (300 mg, 0.378 mmol) as described for **6**. Recrystallization from THF/pentane provided **8** as yellow blocks (285 mg, 56%). IR (KBr) 2960, 2870, 1736, 1699, 1611, 1536, 1464, 1412, 1357, 1220, 1192, 1069, 958, 841, 760, 698, 511 cm^{-1}; UV−vis (CH_2Cl_2) (λ_{max}, nm (ϵ, M^{-1} cm^{-1})) 353 (790). Anal. Calcd for $C_{74}H_{94}N_4O_{12}Fe_2$: C, 66.17; H, 7.05; N, 4.17. Found: C, 66.17; H, 7.01; N, 3.80.

[Fe$_2$(μ-XDK)(μ-O$_2$CAr)(O$_2$CAr)(3-Fpy)$_2$] (9). This compound was prepared from TlO_2CAr (342 mg, 0.757 mmol), 3-fluoropyridine (157 μL, 1.82 mmol), $FeBr_2$ (83 mg, 0.378 mmol), and **4** (300 mg, 0.378 mmol) as described for **6**. Recrystallization from THF/pentane provided **9** as yellow blocks (246 mg, 48%). IR (KBr) 2962, 2931, 2870, 1735, 1697, 1608, 1463, 1409, 1359, 1233, 1197, 1101, 959, 761, 537 cm^{-1}; UV−vis (CH_2Cl_2) (λ_{max}, nm (ϵ, M^{-1} cm^{-1})) 361 (790). Anal. Calcd for $C_{74}H_{92}N_4O_{12}Fe_2F_2$: C, 64.44; H, 6.72; N, 4.06. Found: C, 63.95; H, 6.96; N, 3.53.

[Fe$_2$(μ-BXDK)(μ-O$_2$C*i*-Pr)(O$_2$C*i*-Pr)(py)$_2$] (10). This compound was prepared from TlO_2C*i*-Pr (70 mg, 0.24 mmol), pyridine (60 μL, 0.72 mmol), $FeBr_2$ (26 mg, 0.12 mmol), and **5** (150 mg, 0.120 mmol) as described for **6**. Recrystallization from THF/pentane provided **10** as yellow needles (135 mg, 76%). IR (KBr) 3062, 3028, 2965, 2923, 2869, 1733, 1693, 1602, 1546, 1495, 1446, 1364, 1190, 1034, 850, 763, 701, 528 cm^{-1}; UV−vis (CH_2Cl_2) (λ_{max}, nm (ϵ, M^{-1} cm^{-1})) 357 (920). Anal. Calcd for $C_{86}H_{86}N_4O_{12}Fe_2$: C, 69.82; H, 5.86; N, 3.79. Found: C, 69.34; H, 6.05; N, 3.50.

[Fe$_2$(μ-BXDK)(μ-O$_2$CCH$_2$*t*-Bu)(O$_2$CCH$_2$*t*-Bu)(py)$_2$] (11). This compound was prepared from TlO_2CCH_2*t*-Bu (77 mg, 0.24 mmol), pyridine (60 μL, 0.72 mmol), $FeBr_2$ (26 mg, 0.12 mmol), and **5** (150 mg, 0.120 mmol) as described for **6**. Recrystallization from THF/pentane provided **11** as yellow blocks (130 mg, 71%). IR (KBr) 3062, 3028, 2952, 2866, 1733, 1693, 1603, 1548, 1447, 1364, 1190, 1041, 936, 744, 701, 528 cm^{-1}; UV−vis (CH_2Cl_2) (λ_{max}, nm (ϵ, M^{-1} cm^{-1})) 358 (960). Anal. Calcd for $C_{90}H_{94}N_4O_{12}Fe_2$: C, 70.40; H, 6.17; N, 3.65. Found: C, 70.20; H, 6.60; N, 3.26.

[Fe$_2$(μ-BXDK)(μ-O$_2$CPh)(O$_2$CPh)(py)$_2$] (12). This compound was prepared from TlO_2CPh (78 mg, 0.24 mmol), pyridine (60 μL, 0.72 mmol), $FeBr_2$ (26 mg, 0.12 mmol), and **5** (150 mg, 0.120 mmol) as described for **6**. Recrystallization from THF/CH_2Cl_2/pentane provided **12** as yellow blocks (132 mg, 71%) which appeared suitable for X-ray crystallography. IR (KBr) 3061, 3028, 2952, 2920, 2865, 1733, 1694, 1604, 1543, 1495, 1447, 1364, 1189, 1069, 1042, 937, 853, 762, 720, 701, 588, 528 cm^{-1}; UV−vis (CH_2Cl_2) (λ_{max}, nm (ϵ, M^{-1} cm^{-1})) 351 (1400). Anal. Calcd for $C_{93}H_{84}N_4O_{12}Fe_2Cl_2$ (**12**·CH_2Cl_2): C, 68.43; H, 5.19; N, 3.43. Found: C, 68.84; H, 5.21; N, 3.13.

[Fe$_2$(μ-BXDK)(μ-O$_2$CPhCy)(O$_2$CPhCy)(py)$_2$] (13). This compound was prepared from TlO_2CPhCy (391 mg, 0.960 mmol), pyridine (233 μL, 2.88 mmol), $FeBr_2$ (106 mg, 0.480 mmol), and **5** (600 mg, 0.480 mmol) as described for **6**. Recrystallization from CH_2Cl_2/THF/pentane provided **13** as yellow blocks (623 mg, 76%) which appeared suitable for X-ray crystallography. IR (KBr) 3061, 3028, 2920, 2856, 1735, 1696, 1605, 1494, 1452, 1398, 1366, 1191, 1073, 1042, 864, 762, 699, 526 cm^{-1}; UV−vis (CH_2Cl_2) (λ_{max}, nm (ϵ, M^{-1} cm^{-1})) 354 (940). Anal. Calcd for $C_{104}H_{102}N_4O_{12}Fe_2$: C, 72.98; H, 6.01; N, 3.27. Found: C, 72.73; H, 6.09; N, 3.02.

[Fe$_2$(μ-BXDK)(μ-O$_2$CAr)(O$_2$CAr)(py)$_2$] (14). This compound was prepared from TlO_2CAr (108 mg, 0.240 mmol), pyridine (60 μL, 0.72 mmol), $FeBr_2$ (26 mg, 0.12 mmol), and **5** (150 mg, 0.120 mmol) as described for **6**. Recrystallization from benzene/pentane provided **14** as yellow blocks (144 mg, 67%). IR (KBr) 3068, 3028, 2960, 2928, 2868, 1733, 1693, 1605, 1462, 1406, 1362, 1190, 1070, 937, 762, 701, 730, 528 cm^{-1}; UV−vis (CH_2Cl_2) (λ_{max}, nm (ϵ, M^{-1} cm^{-1})) 352 (870). Anal. Calcd for $C_{110}H_{118}N_4O_{12}Fe_2$: C, 73.41; H, 6.61; N, 3.11. Found: C, 72.96; H, 7.10; N, 3.03.

[Fe$_2$(μ-XDK)(μ-O$_2$CPhCy)(O$_2$CPhCy)(Me-Im)$_2$] (15). To a stirred suspension of Tl_2(XDK) (420 mg, 0.425 mmol) and Me-Im (71 μL, 0.89 mmol) in THF (5 mL) was added $FeBr_2$ (187 mg, 0.851 mmol) in THF (2 mL) followed by TlO_2CPhCy (347 mg, 0.851 mmol) in THF (2 mL). After 12 h the mixture was allowed to settle and the majority of the precipitated TlBr was removed by filtration through Celite. The resulting cloudy filtrate was evaporated to dryness and taken up in benzene. Filtration through Celite afforded a clear filtrate. The Celite/TlBr filter cakes were extracted twice with THF (5 mL) to obtain additional product. The combined filtrate was evaporated to dryness to yield a white residue. This material was suspended in pentane (10 mL), and the resulting white powder was isolated by filtration. Recrystallization from THF/pentane afforded **15** as colorless needles (386 mg, 72%). IR (KBr) 2959, 2929, 2859, 1734, 1695, 1609, 1535, 1462, 1405, 1357, 1228, 1192, 1087, 958, 852, 762, 697, 628 cm^{-1}. Anal. Calcd for $C_{66}H_{80}N_6O_{12}Fe_2$: C, 62.86; H, 6.39; N, 6.66. Found: C, 62.66; H, 6.79; N, 6.00.

[Fe$_2$(μ-PXDK)(μ-O$_2$CPhCy)(O$_2$CPhCy)(Bu-Im)$_2$] (16). This compound was prepared from Tl_2(PXDK) (788 mg, 0.682 mmol), Bu-Im (184 μL, 1.40 mmol), $FeBr_2$ (300 mg, 1.36 mmol), and TlO_2CPhCy (556 mg, 1.36 mmol) as described for **15**. Recrystallization from Et_2O/pentane at −30 °C provided **16** as colorless needles (737 mg, 71%). Recrystallization from a highly dilute pentane solution over several days at room temperature yielded colorless blocks which allowed the compound to be characterized by X-ray crystallography. IR (KBr) 3127, 2959, 2872, 1734, 1693, 1612, 1526, 1456, 1371, 1246, 1187, 1109, 948, 828, 763, 697, 660, 574 cm^{-1}. Anal. Calcd for $C_{84}H_{116}N_6O_{12}Fe_2$: C, 66.66; H, 7.72; N, 5.55. Found: C, 65.13; H, 7.81; N, 5.14.

Collection and Reduction of X-ray Data. Data were collected on a Siemens CCD X-ray diffraction system controlled by a Pentium-based PC running the SMART software package.[31] All crystals were

(31) *SMART*; Version 4.0, Siemens Industrial Automation, Inc.: Madison, WI, 1995.

Table 2. Summary of X-ray Crystallographic Data

	6·CH_2Cl_2	**7**·2.5PhH	**12**·$2CH_2Cl_2$·0.5THF	**13**·3PhH	**16**
formula	$C_{89}H_{92}N_4O_{12}Fe_2Cl_2$	$C_{83}H_{93}N_4O_{12}Fe_2$	$C_{96}H_{90}N_4O_{12.5}Fe_2Cl_4$	$C_{122}H_{120}N_4O_{12}Fe_2$	$C_{84}H_{116}N_6O_{12}Fe_2$
fw	1592.27	1450.38	1753.22	1945.92	1513.53
space group	$P\bar{1}$	$P\bar{1}$	$P\bar{1}$	$P2_1/n$	$P\bar{1}$
a, Å	13.1316(2)	14.7993(3)	14.0207(2)	21.1197(11)	13.2699(2)
b, Å	17.1922(1)	15.5674(3)	16.78920(10)	17.9106(9)	14.09470(10)
c, Å	19.0528(1)	18.0666(3)	19.3547(3)	27.8373(14)	23.0607(4)
α, deg	96.764(1)	88.8330(10)	96.1947(9)		97.1800(10)
β, deg	104.042(1)	81.5630(10)	102.8972(8)	103.6300(10)	97.3300(10)
γ, deg	96.712(1)	70.7380(10)	96.2151(9)		106.4840(10)
V, Å^3	4096.30(7)	3885.02(13)	4373.79(10)	10233.4(9)	4042.74(10)
Z	2	2	2	4	2
ρ_{calcd}, g cm^{-3}	1.291	1.266	1.331	1.263	1.243
T, °C	−85	−85	−85	−85	−85
μ(Mo Kα), mm^{-1}	0.483	0.437	0.518	0.349	0.422
transmission coeff	0.857−1.000	0.788−1.000	0.858−1.000	0.791−1.000	0.871−1.000
2θ limits, deg	3−46	3−57	3−57	3−57	3−57
total no. of data	17736	22684	25335	40431	25104
no. of unique data	11368	16152	17952	14536	17409
obsd data[a]	9221	13216	13809	9120	12887
no. of parameters	982	897	1025	1231	937
R (%)[b]	4.48	4.59	8.81	7.52	5.18
*wR*2 (%)[c]	10.95	12.94	25.18	15.56	12.99
max, min peaks, e Å^{-3}	0.656, −0.506	1.046, −0.385	1.247, −1.533	0.752, −0.361	1.056, −0.597

[a] Observation criterion: $I > 2\sigma(I)$. [b] $R = \sum||F_o| - |F_c||/\sum|F_o|$. [c] $wR2 = \{\sum[w(F_o^2 - F_c^2)^2]/\sum[w(F_o^2)^2]\}^{1/2}$.

mounted on the tips of glass fibers with Paratone-N (Exxon) and cooled to low temperature (∼−85 °C). The general procedures for data collection and reduction follow those reported previously.[32] All structures were solved by use of the direct methods programs SIR-92[33] or XS, part of the TEXSAN[34] and SHELXTL[35] program packages, respectively. Structure refinements were carried out with XL, part of the SHELXTL program package.[35] All non-hydrogen atoms were located and their positions refined by a series of least-squares cycles and Fourier syntheses. Hydrogen atoms were assigned idealized positions and given a thermal parameter 1.2 times the thermal parameter of the carbon atom to which each was attached. Empirical absorption corrections were calculated and applied for each structure with use of the SADABS program.[35]

The structure of **7** contains a lattice benzene molecule that was refined at partial occupancy. Two of the three lattice benzene molecules in the structure of **13** have large thermal parameters. The structure of **12** contains a lattice THF molecule disordered over two positions, where an inversion center passes through the center of a carbon−carbon bond. It was refined as a cyclopentane molecule with one of the carbon atoms at full occupancy, and the occupancy of the other three carbon atoms was distributed over two positions per atom and refined. The butyl group of one of the Bu-Im ligands in the structure of **16** is disordered. The occupancy of the carbon atom β to the imidazole nitrogen atom was distributed over two positions and refined. The other carbon atoms of the butyl group were refined at full occupancy.

Pertinent crystallographic information for each complex including refinement residuals is available in Table 2. All bond distances and angles, as well as atomic coordinates and equivalent isotropic displacement parameters, are provided in Tables S1-S25 (Supporting Information, CIF format).

Physical Measurements. NMR spectra were recorded on a Varian Unity-300 NMR spectrometer. ^{1}H NMR chemical shifts are reported versus tetramethylsilane and referenced to the residual solvent peak. FTIR spectra were recorded on a BioRad FTS-135 FTIR spectrometer. Room-temperature UV−vis spectra were recorded on a Cary 1E spectrophotometer. Low-temperature spectra were recorded on a HP8452A diode array spectrophotometer with a custom manufactured immersion dewar, equipped with a 3-mL cell (1-cm path length) with quartz windows connected to a 14/20 female joint via a 10-cm glass tube. A temperature of −77 °C was maintained with a dry ice/acetone bath and monitored with a Sensortek Model BAT-12 thermocouple thermometer. Conductivity measurements were carried out in THF or CH_2Cl_2 with a Fisher Scientific conductivity bridge, model 9-326, outfitted with a platinum black electrode. Manometric experiments were performed according to a literature procedure,[36] using [IrCl(CO)(PPh$_3$)$_2$] or [FeTp$^{3,5-i\mathrm{Pr}_2}$(O$_2$CCH$_2$Ph)][18] as authentic standards, which form 1:1 and 2:1 complex:O_2 adducts, respectively (Table 3).

Table 3. Manometric Data on Dioxygen Uptake by **13**, **16**, and [Fe(Tp$^{3,5-i\mathrm{Pr}_2}$)(O$_2$CCH$_2$Ph)][a]

		O_2 Uptake (equiv)	
complex	solvent	peroxo formation	peroxo decay
[IrCl(CO)(PPh$_3$)$_2$]	CH_2Cl_2	1.0	
13	CH_2Cl_2	1.0 ± 0.1	0.7 ± 0.1
[Fe(Tp$^{3,5-i\mathrm{Pr}_2}$)(O$_2$CCH$_2$Ph)]	THF	0.55 ± 0.1	0.3 ± 0.1
[Fe(Tp$^{3,5-i\mathrm{Pr}_2}$)(O$_2$CCH$_2$Ph)]	Et_2O	0.45 ± 0.1	0
16	THF	0.9 ± 0.1	1.0 ± 0.1
16	Et_2O	1.0 ± 0.1	0

[a] All O_2 uptake values are in equivalents normalized to the amount of O_2 taken up by an equimolar quantity of [IrCl(CO)(PPh$_3$)$_2$] under identical conditions. $T = -77$ °C for the formation and 22 °C for the decay. In each case, following decay, the system was brought back to equilibrium at −77 °C for the final pressure reading.

EPR Spectroscopy. Spectra were recorded at 4.5 K on a Bruker Model 300 ESP X-band spectrometer operating at 9.47 GHz. Liquid helium temperatures were maintained with an Oxford Instruments EPR 900 cryostat. For all measurements, 1 mM frozen solutions were prepared in 2-methyltetrahydrofuran.

Resonance Raman Spectroscopy. Raman data were acquired by using a Coherent Innova 90 Kr$^+$ laser with an excitation wavelength of 647.1 nm and 65 mW of power. A 0.6-m single monochromator (1200 grooves/nm grating), with an entrance slit of 100 μm, and a liquid nitrogen-cooled CCD detector (Princeton Instruments) were used in a standard backscattering configuration. A holographic notch filter (Kaiser Optical Systems) was employed to attenuate Rayleigh scattering.

(32) Feig, A. L.; Bautista, M. T.; Lippard, S. J. *Inorg. Chem.* **1996**, *35*, 6892.

(33) Burla, M. C.; Camalli, M.; Cascarano, G.; Giacovazzo, C.; Polidori, G.; Spagna, R.; Viterbo, D. *J. Appl. Crystallogr.* **1989**, *22*, 389.

(34) *TEXSAN: Single-Crystal Structure Analysis Software*; Molecular Structure Corporation: The Woodlands, TX, 1995.

(35) *SHELXTL: Structure Analysis Program*, 5.0; Siemens Industrial Automation, Inc.: Madison, WI, 1995.

(36) Mahapatra, S.; Halfen, J. A.; Wilkinson, E. C.; Pan, G.; Wang, X.; Young, V. G., Jr.; Cramer, C. J.; Que, L., Jr.; Tolman, W. B. *J. Am. Chem. Soc.* **1996**, *118*, 11555.

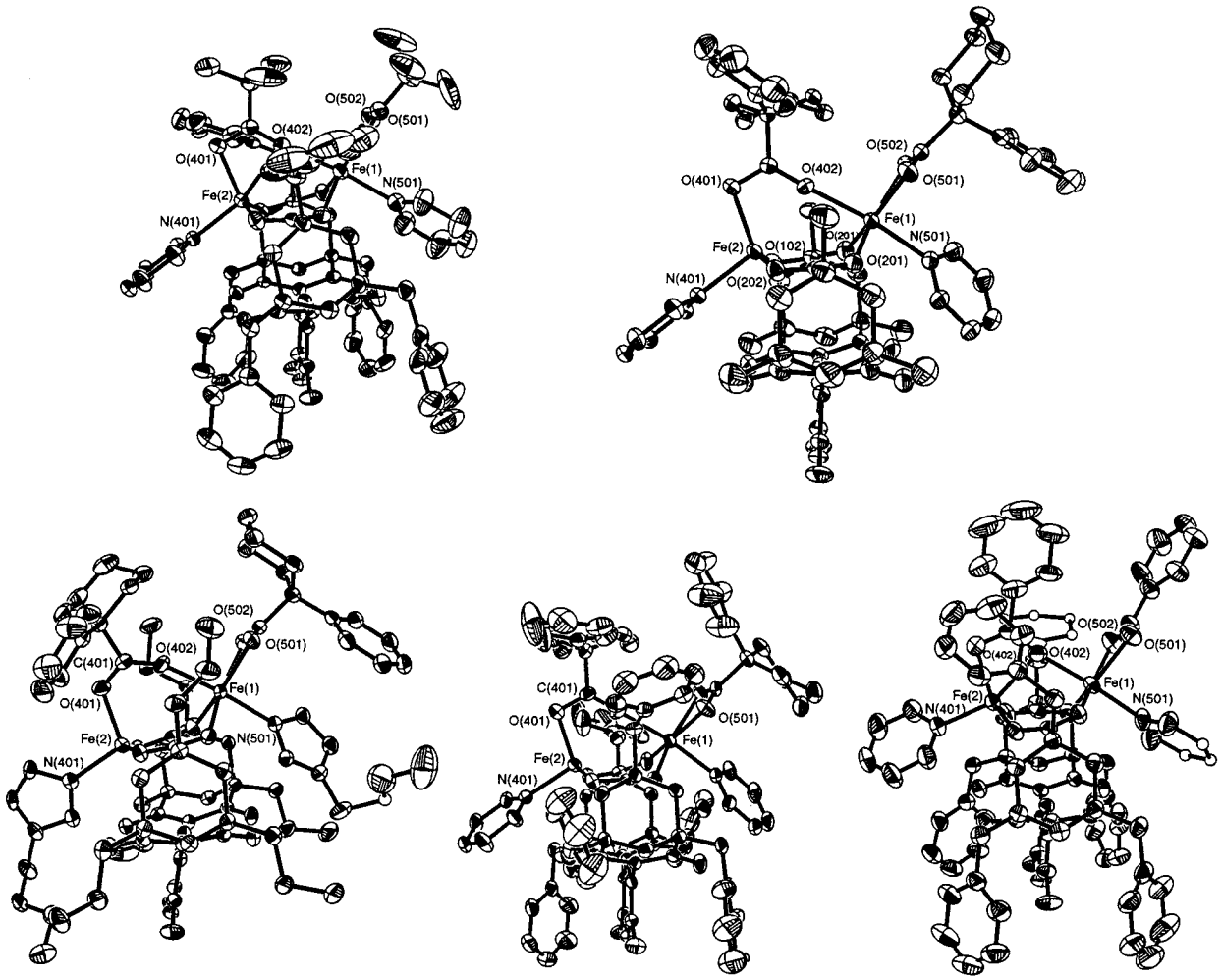

Figure 2. ORTEP diagrams with 50% thermal ellipsoids (clockwise from top left): $[Fe_2(\mu\text{-BXDK})(\mu\text{-}O_2Ct\text{-Bu})(O_2Ct\text{-Bu})(py)_2]$ (**6**), $[Fe_2(\mu\text{-XDK})(\mu\text{-}O_2CPhCy)(O_2CPhCy)(py)_2]$ (**7**), $[Fe_2(\mu\text{-BXDK})(\mu\text{-}O_2CPh)(O_2CPh)(py)_2]$ (**12**), $[Fe_2(\mu\text{-BXDK})(\mu\text{-}O_2CPhCy)(O_2CPhCy)(py)_2]$ (**13**), and $[Fe_2(PXDK)(\mu\text{-}O_2CPhCy)(O_2CPhCy)(Bu\text{-}Im)_2]$ (**16**).

Spectra of all samples were collected in toluene or CH_2Cl_2 solution at −77 °C with the same custom-manufactured dewar used to acquire low-temperature UV−vis spectra. Solutions were made as concentrated as possible, ∼20 mM in the best cases, to ensure an optimal signal-to-noise ratio. A total of 1000 scans, each with a 3-s exposure time, were collected for each sample. Raman shifts were calibrated with toluene or CH_2Cl_2 as an internal standard. The data were processed by using CSMA software (Princeton Instruments, Version 2.4A) on a Gateway 2000 computer, and the resulting ASCII files were processed with Kaleidagraph (Abelbeck Software). Spectra are displayed in Figure 6, and O−O stretching frequencies are listed in Table 4.

Mössbauer Spectroscopy. Solid samples were prepared by suspending ∼0.04 mol of powdered material in Apiezon N grease and then packing the mixture into a nylon sample holder. Frozen solution samples of diferrous complexes **13** and **15** were prepared in THF in a drybox. In each case, 1 mL of an ∼40 mM solution was syringed into a nylon sample holder, which was then sealed with Apiezon N grease and rapidly frozen in liquid nitrogen. The peroxo derivative of **13** was prepared in a round-bottom flask at −77 °C by exposing 1 mL of a THF solution of **13** (40 mM) to excess O_2 (1 atm) for 2 h. The sample was quickly transferred (<5 s) into a nylon sample holder, immersed in liquid nitrogen, by means of a glass syringe equipped with a 4-cm stainless steel needle that had been precooled to −77 °C. All data were collected at 77 K with a ^{57}Co source in a Rh matrix at room temperature and fit to Lorentzian line shapes. Spectra are illustrated in Figure 7, and parameters derived from the fits are listed in Table 5.

UV−Vis Kinetics. Experiments were carried out by using the custom dewar mentioned above. Reduced samples in freshly distilled THF solution, typically 0.5 mM, were loaded in a drybox, and the dewar was fitted with a rubber septum. The apparatus was brought out, placed under a positive N_2 pressure, and cooled to −77 °C with a dry ice/acetone bath. The samples were subjected to an O_2 purge at atmospheric pressure for 5.0 min at a flow rate of 10 standard cubic centimeters per minute (SCCM), maintained with a Matheson Dyna-Blender Model 8280 oxygen/nitrogen constant flow mixing system. Purging for this time length and at this flow rate resulted in highly reproducible rate constants, thus ensuring that the entire sample solution and vessel headspace had been completely purged with the desired gas mixture. For dioxygen-dependent kinetic studies, the mole fraction of O_2 was controlled by diluting pure O_2 with N_2, while retaining a total flow rate of 10 SCCM. Dioxygen concentrations were calculated by using eq 4, where X = mole fraction of O_2, L = Ostwald coefficient

$$X = \left(\frac{RT}{P_{(g)}LV^{\circ}_{(1)}} + 1\right)^{-1} \tag{4}$$

(0.245 for THF), $P_{(g)}$ = partial pressure, and $V^{\circ}_{(1)}$ = molar volume.[37] All experiments were carried out under pseudo-first-order dioxygen concentrations, ranging from 3.07 to 15.4 mM, while keeping the initial concentration of diferrous complex constant. Absorbance values were measured at 600 nm every 2−10 s, depending on the rate at which the reaction proceeded. Reactions were followed to at least 4 half-lives in all cases. Data were analyzed with Kaleidagraph (Abelbeck Software) and fit to model-dependent equations by using nonlinear least-squares regression. In all cases the data were fit unambiguously to a

(37) *Oxygen and Ozone*; Battino, R., Ed.; Pergamon Press: Oxford, U.K., 1981; Vol. 7.

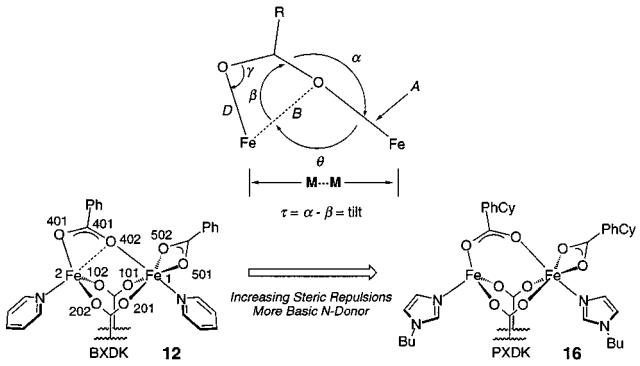

	12	6	7	13	16
XDK Deriv.	BXDK	BXDK	XDK	BXDK	PXDK
Ancil. Carbox.	Ph	*t*-Bu	PhCy	PhCy	PhCy
N-Donor	py	py	py	py	Bu-Im
M ··· M	3.5121(8)	3.5110(6)	3.5932(4)	3.5649(10)	3.6671(5)
B = Fe2–O402	2.317(3)	2.340(2)	2.454(2)	2.489(4)	3.055(2)
D = Fe2–O401	2.047(4)	2.062(2)	2.050(2)	2.017(4)	2.006(4)
A = Fe1–O402	2.184(3)	2.172(2)	2.217(2)	2.194(4)	2.154(2)
θ = Fe1–O402–Fe2	102.55(12)	102.13(9)	100.47(6)	98.96(13)	87.72(6)
α = Fe1–O402–C401	168.9(3)	170.6(2)	171.5(2)	168.0(3)	152.6(2)
γ = Fe2–O401–C401	96.3(3)	97.5(2)	100.15(13)	101.5(3)	116.6(2)
β = Fe2–O402–C401	84.6(3)	84.5(2)	81.84(12)	80.3(3)	67.46(15)
$\tau = \alpha - \beta$	73	73	71	66	36

Figure 3. A schematic illustration of the effect of ligand substituent steric repulsion on the orientation of the bridging ancillary carboxylate, including the relevant metrical parameters which account for this effect.

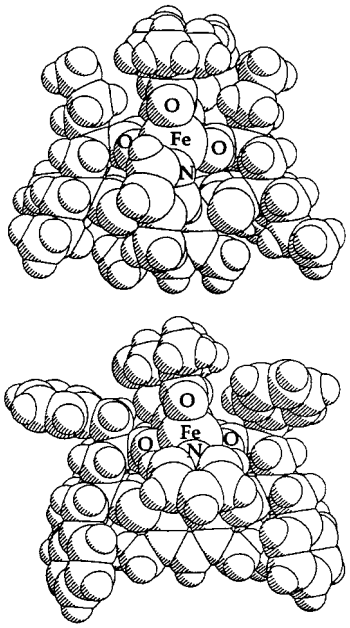

Figure 4. Space-filling representations of [Fe_2(μ-PXDK)(μ-O_2C*t*-Bu)(O_2C*t*-Bu)(Me-Im)$_2$] from ref 23 (top) and [Fe_2(μ-BXDK)(μ-O_2C*t*-Bu)(O_2C*t*-Bu)(py)$_2$] (**6**) (bottom), looking down the Fe···Fe vector.

first-order exponential buildup, defined in eq 5, where A_t is the

$$A_t = A_\infty + (\Delta A)(1 - \exp(-k_{obs}t)) \quad (5)$$

$$\text{rate} = k[\text{Fe}^{\text{II}}{}_2][O_2] \quad (6)$$

absorbance at time *t*, ΔA is the change in absorbance during the reaction,

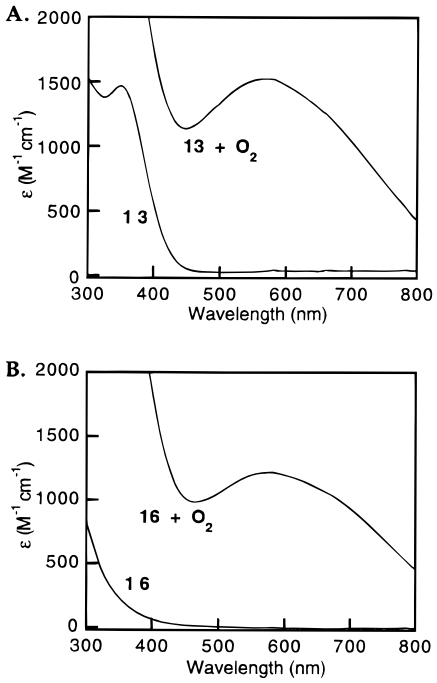

Figure 5. Representative UV−vis spectra for the reaction of diferrous complexes **6**−**15** with O_2 at −77 °C in THF: (A) [Fe_2(μ-BXDK)(μ-O_2CPhCy)(O_2CPhCy)(py)$_2$] (**13**) and (B) [Fe_2(μ-PXDK)(μ-O_2CPhCy)-(O_2CPhCy)(Bu-Im)$_2$] (**16**).

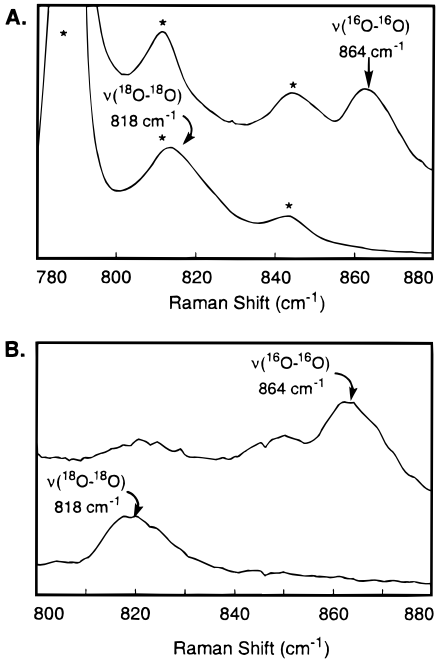

Figure 6. Resonance Raman spectra obtained with 647-nm excitation at −77 °C on fluid solutions in toluene of (A) [Fe_2($^{16}O_2$)(μ-PXDK)(O_2-CPhCy)$_2$(Bu-Im)$_2$] (top) and [Fe_2($^{18}O_2$)(μ-PXDK)(O_2CPhCy)$_2$(Bu-Im)$_2$] (bottom). Peaks marked with an asterisk are due to solvent. Solvent-subtracted spectra normalized to the 788-cm^{-1} toluene peak are shown in part B.

A_∞ is the absorbance at infinite time, and k_{obs} ($\equiv k_\psi$) is the observed pseudo-first-order rate constant. All plots of ln(k_{obs}) vs ln([O_2]) were linear with a slope close to 1.0, implying that an overall second-order rate law applies, eq 6. Second-order rate constants, listed in Table 6, were derived from the slopes of k_{obs} vs [O_2] plots. Standard errors in these rates are based on linear regression analyses of the slopes and are reported at the 95% confidence level. Plots of *A* (at 600 nm) vs *t*, k_ψ vs [O_2], and ln(k_ψ) vs ln([O_2]) for complexes **6**, **7**, **13**, and **14** are

Table 4. Summary of Resonance Raman Data for the Peroxo Adducts

compound	solvent	$\nu(^{16}O-^{16}O)$ ($^{18}O_2$)
$[Fe_2(O_2)(\mu\text{-BXDK})(O_2Ct\text{-Bu})_2(py)_2]$	toluene	864
$[Fe_2(O_2)(\mu\text{-XDK})(O_2CPhCy)_2(py)_2]$	toluene	864
$[Fe_2(O_2)(\mu\text{-XDK})(O_2CAr)_2(py)_2]$	toluene	864
$[Fe_2(O_2)(\mu\text{-BXDK})(O_2CPhCy)_2(py)_2]$	toluene	864
$[Fe_2(O_2)(\mu\text{-BXDK})(O_2CPhCy)_2(py)_2]$	CH_2Cl_2	861 (811)
$[Fe_2(O_2)(\mu\text{-BXDK})(O_2CAr)_2(py)_2]$	toluene	864
$[Fe_2(O_2)(\mu\text{-PXDK})(O_2CPhCy)_2(Bu\text{-Im})_2]$	toluene	864 (818)

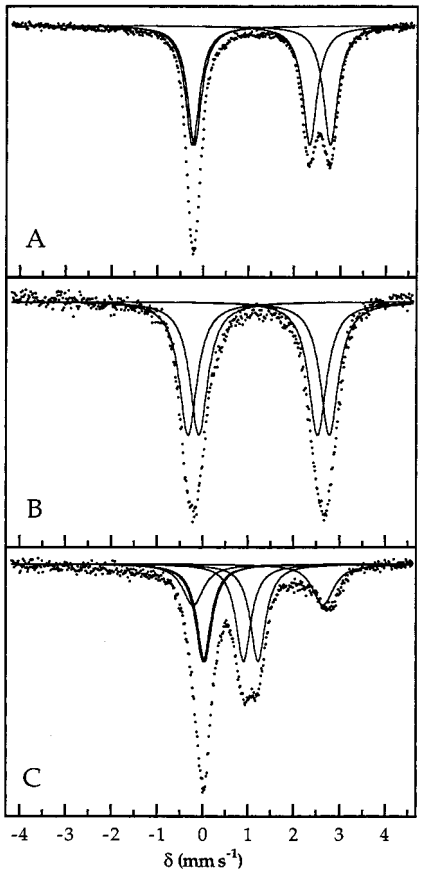

Figure 7. Zero-field Mössbauer spectra (experimental data (•), calculated fit (−)) recorded at 77 K for $[Fe_2(\mu\text{-BXDK})(\mu\text{-}O_2CPhCy)(O_2CPhCy)(py)_2]$ (**13**) in the solid state (A), in THF solution (B), and after exposure to dioxygen in THF solution (C). The diferrous component in spectrum C was approximated as a single quadrupole doublet.

provided in Figures 8 and S6−S8 (see Supporting Information for Figures S6−S8), respectively.

Results and Discussion

Preparation and Characterization of [Fe(XDK)(py)$_2$] (4) and [Fe(BXDK)(py)$_2$] (5). To develop an efficient synthetic route to a family of diiron(II) complexes incorporating XDK and related ligands, as well as ancillary carboxylates of variable steric demands, access to large amounts of pure mononuclear precursors was desired. Treatment of Tl_2(XDK) or Tl_2(BXDK) with 1 equiv of iron(II) bromide and excess pyridine provided yellow bis(pyridine) adducts **4** and **5**, respectively, in multigram quantities and high yield (eq 7). An X-ray structural analysis of the XDK derivative revealed the iron atom to be coordinated

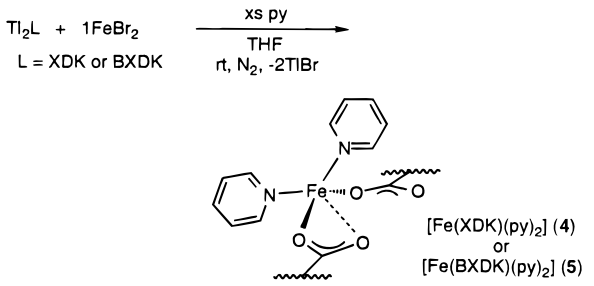

(7)

by three carboxylate oxygen and two pyridine nitrogen atoms.[38] The structure is essentially identical to that determined for the Zn(II) analogue,[39] with one long Fe−O_{XDK} interaction at 2.326(5) Å and the other two at an average distance of 2.080(3) Å. In contrast, the analogous reaction with 1-methyl- or 1-butylimidazole led to an intractable mixture of products, even when exactly 2 equiv were used.

Preparation and Characterization of Dinuclear [Fe$_2$(μ-BXDK)(μ-O$_2$C*t*-Bu)(O$_2$C*t*-Bu)(py)$_2$] (6), [Fe$_2$(μ-XDK)(μ-O$_2$CPhCy)(O$_2$CPhCy)(py)$_2$] (7), [Fe$_2$(μ-XDK)(μ-O$_2$CAr)(O$_2$CAr)(py)$_2$] (8), [Fe$_2$(μ-XDK)(μ-O$_2$CAr)(O$_2$CAr)(3-Fpy)$_2$] (9), [Fe$_2$(μ-BXDK)(μ-O$_2$C*i*-Pr)(O$_2$C*i*-Pr)(py)$_2$] (10), [Fe$_2$(μ-BXDK)(μ-O$_2$CCH$_2$*t*-Bu)(O$_2$CCH$_2$*t*-Bu)(py)$_2$] (11), [Fe$_2$(μ-BXDK)(μ-O$_2$CPh)(O$_2$CPh)(py)$_2$] (12), [Fe$_2$(μ-BXDK)(μ-O$_2$CPhCy)(O$_2$CPhCy)(py)$_2$] (13), [Fe$_2$(μ-BXDK)(μ-O$_2$CAr)(O$_2$CAr)(py)$_2$] (14), [Fe$_2$(μ-XDK)(μ-O$_2$CPhCy)(O$_2$CPhCy)(Me-Im)$_2$] (15), and [Fe$_2$(μ-PXDK)(μ-O$_2$CPhCy)(O$_2$CPhCy)(Bu-Im)$_2$] (16). The diferrous bis(pyridine) complexes **6**−**14** were conveniently prepared from **4** or **5** and "[Fe(O$_2$CR)$_2$(py)$_n$]", the latter being generated in situ from iron(II) bromide, the thallium(I) salts of the corresponding ancillary carboxylate, and excess pyridine (eq 8). The 3-fluoropyridine derivative **9** and imidazole adducts **15** and **16** were prepared in one-pot reactions from the thallium carboxylates, 2 equiv of iron(II) bromide, and 2 equiv of 3-fluoropyridine or 1-alkylimidazole. In the synthesis of **15** and **16**, removal of solid TlBr was aided by allowing the reaction mixtures to stand overnight prior to filtration through

Table 5. Zero-Field Mössbauer Parameters for $[Fe_2(\mu\text{-BXDK})(\mu\text{-}O_2CPhCy)(O_2CPhCy)(py)_2]$ (**13**), $[Fe_2(\mu\text{-XDK})(\mu\text{-}O_2CPhCy)(O_2CPhCy)(Me\text{-}Im)_2]$ (**15**), $[Fe_2(O_2)(\mu\text{-BXDK})\text{-}(O_2CPhCy)_2(py)_2]$, Oxyhemerythrin, and $MMOH_{peroxo}$

complex	T (K)	δ (mm s^{-1})	ΔE_Q (mm s^{-1})	Γ (mm s^{-1})	ref
13 (powder)	77	1.06	2.56	0.37	*a*
		1.28	3.01	0.37	
13 (THF)	77	1.10	2.85	0.48	*a*
		1.34	2.87	0.48	
15 (THF)	77	1.14	2.98	0.45	*a*
		1.36	2.94	0.45	
$[Fe_2(O_2)(\mu\text{-BXDK})(O_2CPhCy)_2(py)_2]$	77	0.47	0.88	0.40	*a*
		0.63	1.20	0.40	
Oxyhemerythrin	77	0.50	2.02	∼0.3	43
		0.51	1.01	∼0.3	
$MMOH_{peroxo}$	4.2	0.66	1.51	0.27	15

[a] This work.

Table 6. Correlation of Rate Constant of Peroxodiiron(III) Complex Formation at −77 °C, with Tilt Angle (τ) Measured in the Solid State

	complex			
parameter	**6**	**7**	**13**	**14**
k (M^{-1} s^{-1})	0.0398 ± 0.0009	0.045 ± 0.003	0.16 ± 0.01	0.115 ± 0.005
τ (deg)[a]	73	71	66	*b*

[a] See Figure 4 for a definition of τ. [b] An X-ray structure was determined for **14**, but it was of insufficient quality for an accurate measurement of bond distances and angles.

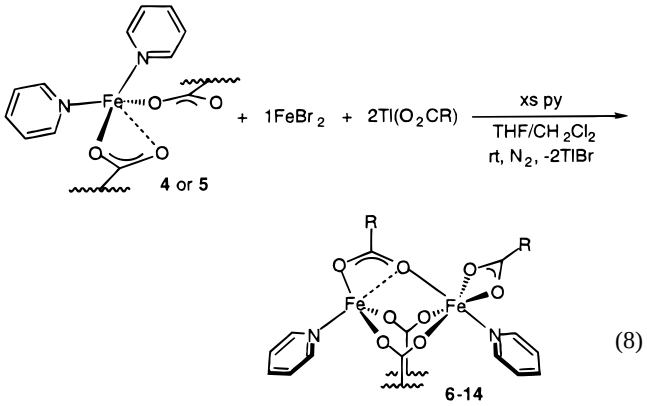

(8)

Celite. Further extractions of the resulting Celite/TlBr filter cake were required to recover substantial quantities of additional product. All complexes were obtained in high yield and purity following recrystallization at room temperature. Despite repeated attempts in each case, elemental analyses for samples of **4**, **7**, and **16** deviated by 1−2% from the calculated carbon values. It is unclear whether these complexes have poor combustion properties or contain minor quantities of impurities, but other closely related derivatives gave satisfactory analyses. Structural diagrams of **4**−**16** are provided in Scheme 1.

The IR spectra of **7**−**16** displayed C−O stretches between 1602 and 1614 cm^{-1} and another centered at ∼1693 cm^{-1}, which was more intense and broadened compared to that in either the dithallium(I) or mononuclear iron(II) precursors. Both features are attributed to the two additional carboxylate ligands in the products. The UV−vis spectra of the pyridine adducts **4**−**14** all exhibited an absorbance at ∼360 nm (ϵ = 500−1000 M^{-1} cm^{-1}), tentatively assigned as a metal-to-ligand charge-transfer band, which was absent in the colorless 1-alkylimidazole derivatives. Complexes **4**−**16** are all nonelectrolytes, and most are soluble in solvents as nonpolar as THF. Complex **16**, with its highly saturated hydrocarbon periphery, is readily soluble in diethyl ether and cyclopentane.

The ability to acquire X-ray crystal structures of **6**, **7**, **12**, **13**, and **16** has enabled us to ascertain how each ligand component, with its particular steric and electronic properties, might influence the iron coordination geometries and, ultimately, dioxygen reactivity of the complexes. ORTEP and space-filling diagrams of these compounds are displayed in Figures 2 and 4, respectively, and selected bond distances and angles are listed in Figure 3. Each structure consists of one six-coordinate and one four- or five-coordinate iron atom. The number of donor atoms on the coordinatively unsaturated iron center (Fe2) depends on the choice of N-donor ligand and the stereochemical demands of the XDK and ancillary carboxylates. The Fe2 atoms in **6** and **12** are best described as distorted trigonal bipyramidal,

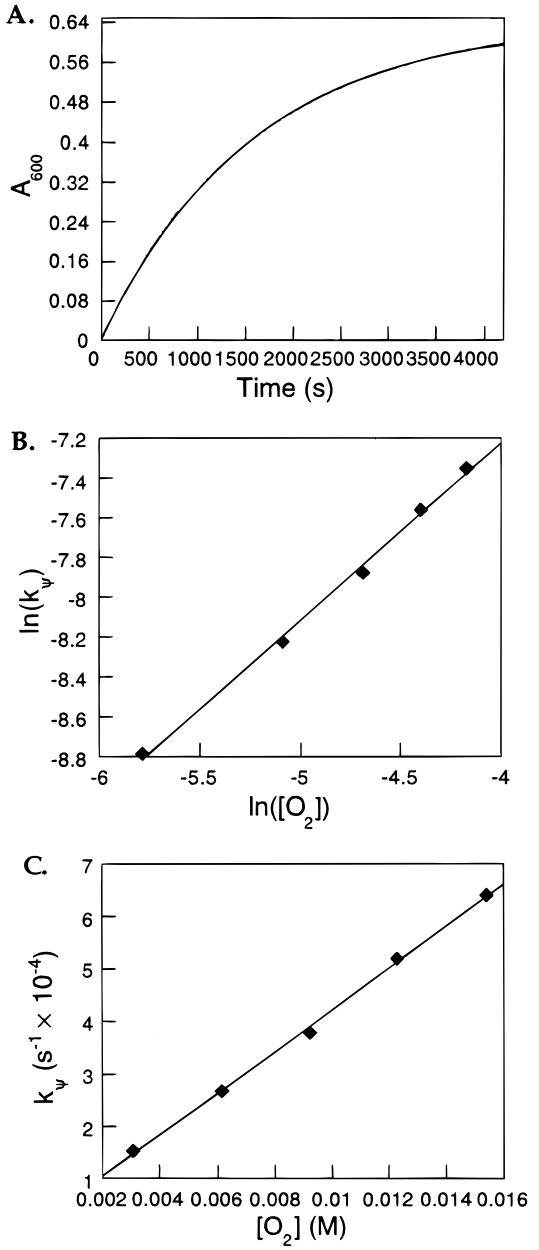

Figure 8. Kinetic data for the reaction of [Fe_2(μ-BXDK)(μ-O_2C*t*-Bu)(O_2C*t*-Bu)(py)$_2$] (**6**) with O_2 in THF at −77 °C: (A) plot of A_{600} vs t with $[\mathbf{6}]_0$ = 0.73 mM and $[O_2]$ = 15.4 mM and a fit to a first-order exponential buildup, (B) plot of ln(k_ψ) vs ln($[O_2]$), and (C) plot of k_ψ vs $[O_2]$.

and those in **7**, **13**, and **16** as distorted tetrahedral. The other iron atom (Fe1) adopts a pseudo-octahedral environment comprising two carboxylate oxygen atoms of a *syn*,*syn*-bidentate bridging XDK ligand, two symmetric chelating ancillary carboxylate oxygen atoms, and a nitrogen atom from the N-donor ligand.

The most significant difference in these structures is the orientation of the ancillary bridging carboxylate ligand relative

(38) X-ray data for **4** crystallized from CH_2Cl_2/Et_2O: $P2_1/n$, a = 12.3185(2) Å, b = 16.2489(2) Å, c = 20.4920(1) Å, β = 103.77(1)°, V = 3983.92(8) Å^3, Z = 4, T = 188 K, R = 0.0677, $wR2$ = 0.1372. This structure is not described in further detail here because it is nearly identical to that of the Zn(II) analogue (see ref 39) .

(39) Tanase, T.; Yun, J. W.; Lippard, S. J. *Inorg. Chem.* **1995**, *34*, 4220.

Scheme 1

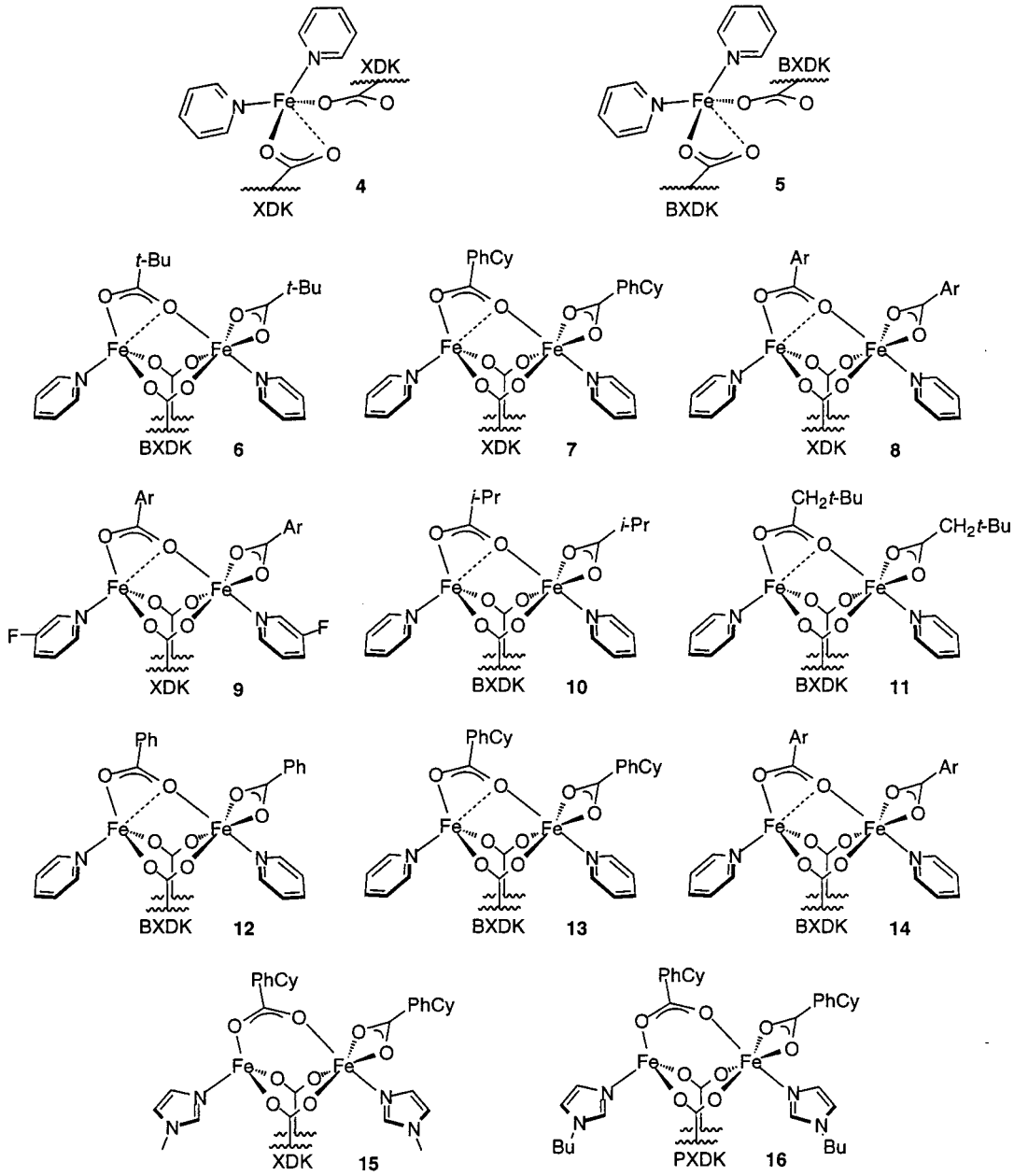

to the rest of the complex framework. Six metrical parameters change significantly within the series, Fe2−O402, Fe2−O401, Fe1−O402−Fe2, Fe1−O402−C401, Fe2−O401−C401, and Fe2−O402−C401. These changes are related to the previously defined tilt angle, τ, of the monodentate bridging carboxylate ligand, as illustrated in Figure 3.[40] Within the subset of pyridine complexes **6**, **7**, **12**, and **13**, repulsive interactions between substituents on the ancillary carboxylate ligands decrease τ. In **12** and **13**, τ is similarly affected by a steric interaction between these substituents and the benzyl groups on BXDK. As the Fe2−O402 bridge distance (*B*) lengthens, the Fe2−O401 dangling distance (*D*) shortens, resulting in little alteration of the Fe1−O402 distance (*A*) across the series. Similarly, an increase in the Fe2−O401−C401 angle (γ) is accompanied by a decrease in the Fe1−O402−Fe2 (θ), Fe1−O402−C401 (α), and Fe2−O402−C401 (β) angles. On the basis of the values of these parameters, the order of increasing steric repulsion between carboxylate substituents for this subset of pyridine complexes is **12** < **6** < **7** < **13**, corresponding to $\Delta\tau = -7°$. By contrast, τ is much smaller for the 1-butylimidazole adduct **16** compared to all of the pyridine complexes. We attribute this property to the more basic character of the 1-alkylimidazole donor compared to pyridine, a factor that increases the electron density at Fe2, thereby completely abrogating the Fe2−O402 interaction. Hence, for **16**, the steric and electronic factors have the combined effect of inducing a nearly complete carboxylate shift[40] from the monodentate bridging mode observed for the pyridine adducts to a *syn,syn*-bidentate bridging mode.

Reactions of the Diferrous Complexes with O_2 To Form Diiron(III) Peroxo Complexes. (a) UV−Vis Studies. Previous work revealed the generation of a short-lived intermediate when [Fe_2(μ-PXDK)(μ-O_2C*t*-Bu)(O_2C*t*-Bu)(Me-Im)$_2$] was exposed to excess O_2 at −77 °C in THF solution.[23] In a first attempt to obtain a more stable derivative, we implemented the more sterically demanding BXDK ligand, while holding the other steric properties constant, and changed the N-donor ligand

(40) Rardin, R. L.; Tolman, W. B.; Lippard, S. J. *New J. Chem.* **1991**, *15*, 417.

to pyridine. Space-filling diagrams of the previously reported complex and **6** are displayed in Figure 4. From these representations, it is apparent that the BXDK benzyl substituents proximal to its carboxylate oxygen donor atoms shield the iron coordination sites to a greater extent than do the PXDK propyl groups. Moreover, the benzyl substituents would tend to direct the approach of the O_2 molecule to the unsaturated metal center along the Fe−Fe vector.

Exposure of **6** to O_2 under conditions identical to those previously reported[23] resulted in a much slower color change to deep midnight blue. The buildup of a broad absorption centered at ∼580 nm ($\epsilon \approx 1200$ M^{-1} cm^{-1}) was monitored by UV−vis spectroscopy over the course of 2−3 h. This feature is characteristic of a peroxo-iron(III) ligand-to-metal charge-transfer transition.[1,5] The oxygenation reaction is irreversible, since application of high vacuum/Ar purge cycles to the solution at −77 °C resulted in no diminution in the intensity of the charge-transfer band. Warming above −65 °C under excess O_2 or Ar, or under high vacuum, however, led to decomposition within 5 min, as judged by a color change to light brown. A similar decomposition was noted when the solution was allowed to stand at −77 °C for 12−24 h.

The other diiron(II) tetracarboxylate complexes were screened for their ability to form stable peroxo complexes. The O_2 reactions either resulted in rapid decomposition to form Fe(III) products or afforded an intermediate very similar to that observed with **6** (Figure 5). For derivatives containing BXDK and pyridine, ancillary carboxylate ligands smaller than pivalate (**10**−**12**) reacted with O_2 at a similar rate, but none of these reactions resulted in buildup of the 580-nm charge-transfer band. The sterically less demanding XDK ligand formed stable peroxo adducts when significantly more hindered ancillary carboxylates were employed, such as in compounds **7** and **8**. These same hindered carboxylates afforded similarly stable peroxo adducts with 3-fluoropyridine as in **9** or 1-alkylimidazole donors as in **15** and **16** (Figure 5B). The rate of peroxo formation was considerably faster for the 1-alkylimidazole complexes compared to all the pyridine analogues, however, with **15** and **16** reacting with O_2 to completion within seconds compared to **6**−**14**, which required 0.25−2 h, as judged by UV−vis spectroscopy. The energy and intensity of the peroxo-to-iron(III) charge-transfer bands in these derivatives were the same as for the pyridine analogues. This result is not surprising because other diiron(III) peroxo complexes with widely varying ligand sets exhibit nearly identical transitions.[1,5] Moreover, none of the peroxo derivatives released O_2 at −77 °C, and all had similarly narrow ranges of thermal stability, irrespective of their rates of formation.

(b) Manometric Studies. Dioxygen uptake was monitored by manometry for the pyridine adduct **13** in CH_2Cl_2 and for the 1-butylimidazole adduct **16** in THF and Et_2O (Table 3). Compounds **13** and **16** consumed 1.0 ± 0.1 equiv of O_2, consistent with formation of discrete diiron(III) peroxide species. When these adducts were allowed to decay by warming them to room temperature, additional O_2 consumption was observed in manometric experiments carried out in CH_2Cl_2 or THF, whereas no further gas uptake occurred for diethyl ether solutions. This behavior contrasts with that previously reported for peroxo-bridged diiron(III) alkoxo complexes,[25] where 0.5 equiv of O_2 was *released* upon peroxo decay, suggesting that, in the systems described here, either the peroxide ligand is retained in the decomposition products or that ligand or solvent oxidation occurs during peroxo decay. A detailed analysis of this chemistry has been undertaken and will be reported elsewhere.[26] Taken together, the results from these steric, electronic, and solvent polarity studies demonstrate that peroxo adducts can be stabilized in this ligand environment provided that the carboxylate substituents afford sufficient steric bulk.

Characterization of the Diiron(III) Peroxo Complexes. (a) EPR and ^{1}H NMR Spectroscopy. The peroxo species described above are EPR silent at 4.5 K, thereby implying antiferromagnetically coupled, $S = 0$ ground states. As with other diiron(III) peroxides, including the H_{peroxo} intermediate of MMOH,[15] such coupling is probably mediated by a bridging peroxide ligand.[41,42] The failure to observe a ^{1}H NMR spectrum for the peroxo adducts in CD_2Cl_2 at −80 °C, however, suggests the presence of low-lying paramagnetic excited states which can be thermally accessed and which induce fast nuclear spin relaxation of the ligand protons. In contrast, a paramagnetically shifted but reasonably sharp ^{1}H NMR spectrum was observed for a diiron(III) peroxo complex having a sterically hindered hydrotris(pyrazolyl)borate ligand.[41]

(b) Resonance Raman Spectroscopy. Raman spectra were acquired for peroxo adducts of **6**−**8**, **13**, **14**, and **16** in fluid solution at −77 °C. The results of these experiments are summarized in Table 4, and the spectra acquired for the peroxo derivative of **16** are displayed in Figure 6. The pyridine and 1-butylimidazole derivatives all exhibit a $\nu(^{16}O-^{16}O)$ band at 864 cm^{-1} in toluene solution. When $^{18}O_2$ was used in the synthesis, this band shifted to 818 cm^{-1}, in good agreement with the theoretically predicted value of 814 cm^{-1} for a diatomic O−O harmonic oscillator. The $\nu(^{16}O-^{16}O)$ peak shifts slightly to 861 cm^{-1} for the peroxide complex of **13** in CH_2Cl_2 solution. An Fe−O stretching frequency could not be assigned in toluene or CH_2Cl_2 due to the presence of peaks from the complex and solvent which obscured this region of the spectrum. The $\nu(^{16}O-^{16}O)$ frequencies of 861−864 cm^{-1} are 15−40 cm^{-1} lower in energy than reported for crystallographically characterized (μ-1,2-peroxo)diiron(III) complexes,[1,5] but 50−60 cm^{-1} higher in energy than those observed in mononuclear η^2-peroxo-iron(III) units.[1] We therefore tentatively assign μ-1,2 coordination modes for the peroxo derivatives of **13** and **16**.

Raman spectroscopy was also used to investigate the possibility that the peroxide ligand might exchange with free O_2. Such a process could be either dissociative (eq 9), implying reversible O_2 binding, or associative (eq 10). The former

$$[Fe^{III}_2(^{18}O_2)(\mu\text{-L})(O_2CR)_2(N)_2] \overset{-^{18}O_2}{\rightleftharpoons} [Fe^{II}_2(\mu\text{-L})(O_2CR)_2(N)_2] \overset{+^{16}O_2}{\rightleftharpoons} [Fe^{III}_2(^{16}O_2)(\mu\text{-L})(O_2CR)_2(N)_2] \quad (9)$$

$$[Fe^{III}_2(^{18}O_2)(\mu\text{-L})(O_2CR)_2(N)_2] \overset{+^{16}O_2}{\rightleftharpoons} [Fe^{III}_2(^{18}O_2)(^{16}O_2)(\mu\text{-L})(O_2CR)_2(N)_2] \overset{-^{18}O_2}{\rightleftharpoons} [Fe^{III}_2(^{16}O_2)(\mu\text{-L})(O_2CR)_2(N)_2] \quad (10)$$

mechanism is unlikely because O_2 was not liberated when a solution of the peroxo adduct was placed under a dynamic vacuum. A sample of the [^{18}O]peroxo derivative of **16** was prepared by exposing a 20 mM solution in toluene to ∼0.25 atm of excess $^{18}O_2$ for 1 h, and resonance Raman spectra were recorded prior to and following a vigorous, 5-min $^{16}O_2$ purge.

(41) Kitajima, N.; Tamura, N.; Amagai, H.; Fukui, H.; Moro-oka, Y.; Mizutani, Y.; Kitagawa, T.; Mathur, R.; Heerwegh, K.; Reed, C. A.; Randall, C. R.; Que, L., Jr.; Tatsumi, K. *J. Am. Chem. Soc.* **1994**, *116*, 9071.

(42) Dong, Y.; Ménage, S.; Brennan, B. A.; Elgren, T. E.; Jang, H. G.; Pearce, L. L.; Que, L., Jr. *J. Am. Chem. Soc.* **1993**, *115*, 1851.

The $\nu(^{16}O-^{16}O)$ feature appeared in the spectrum immediately following the purge, but not at the expense of the intensity of the $\nu(^{18}O-^{18}O)$ band. Moreover, the $\nu(^{16}O-^{16}O)$ peak continued to grow in intensity when the solution was allowed to stir under 1 atm of $^{16}O_2$ over 2 h, but again the $\nu(^{18}O-^{18}O)$ band did not diminish. These results indicate that oxygenation of the reduced complex is slow in the concentrated solutions of **16** required for the Raman experiment and that peroxide does not exchange with free O_2, at least over several hours.

(c) Mössbauer Spectroscopy. Zero-field Mössbauer studies were carried out to gain additional information concerning the environment around the iron centers of the diiron(II) and peroxodiiron(III) complexes. Spectra overlaid with theoretical fits to the data are presented in Figure 7 for **13** and its peroxo derivative. The derived parameters, along with those for oxyhemerythrin[43] and H_{peroxo},[15] are summarized in Table 5.

The Mössbauer spectrum of powdered **13** (Figure 7A) indicates the presence of two distinct high-spin Fe(II) centers, consistent with its X-ray crystal structure (Figure 2). Valence bond theory dictates that the lower-coordinate Fe2 center of **13** will have greater s-orbital character relative to the pseudooctahedral Fe1. Because these two Fe(II) centers are coordinated by similar weak-field ligands, the quadrupole doublet with the smaller isomer shift (1.06 mm s^{-1}) is assigned to Fe2 and the one with the larger isomer shift (1.28 mm s^{-1}) to Fe1. Such an assignment of the two quadrupole doublets to specific iron centers in **13** requires for consistency that the previously reported[23] Mössbauer parameters of less hindered analogues be interchanged. In a separate issue, although one of the sterically less hindered analogues of **13** exhibited nearly identical Mössbauer parameters in both the powdered and frozen solution states,[23] the spectrum of **13** appears different when measured in a frozen THF solution (Figure 7B). The latter spectrum, however, is essentially identical to the frozen solution Mössbauer spectrum of **15**, suggesting that **13** and **15** share very similar structures in solution. The integrated intensities of the two overlapping quadrupole doublets are equal, thereby indicating that the dinuclear structure remains intact in solution.

The Mössbauer spectrum of the peroxo derivative of **13** in frozen THF solution is displayed in Figure 7C. A moderate amount (~20%) of the diiron(II) starting material is detected in this sample, as judged by a comparison of the position of the absorption feature at ~2.8 mm s^{-1} with that observed for **13** (Figure 7B). This result is in accord with the resonance Raman experiment described above, where it was determined that oxygenation of very concentrated (20 mM) diiron(II) samples is slow relative to the rate in more dilute solutions, such as that used for the UV−vis studies. Given the thermal instability of the peroxo complexes, which decompose significantly within 12−24 h at −77 °C, and the fact that the spectroscopic properties of the reduced complexes are well-known, we chose not to allow any of these concentrated reactions to proceed beyond ~2 h.

Figure 7C portrays the experimental data with the diiron(II) component subtracted out, together with a fit to two quadrupole doublets of equal integrated intensity. The isomer shift (0.48 and 0.63 mm s^{-1}) and quadrupole splitting (0.88 and 1.20 mm s^{-1}) values are both within the range for high-spin Fe(III),[44] and resemble those determined for the phenoxo-bridged peroxodiiron(III) complex in Table 1.[19] These results indicate that the peroxo complex of **13** is composed of either a single dinuclear species containing inequivalent iron centers or two distinct dinuclear species with equivalent iron centers within the same molecule. Since the generation of a 1:1 ratio of two different diiron(III) peroxo isomers is unlikely to occur upon addition of O_2 to a solution of **13**, we conclude that the former description best accounts for the nature of this peroxo complex.

Kinetic Studies of the Reaction of the Diferrous Complexes with O_2. (a) Correlation of Kinetic Parameters with Complex Stereochemistry. The UV−vis, manometric, EPR, resonance Raman, and Mössbauer spectroscopic data collectively point to the formation of discrete (μ-1,2-peroxo)diiron(III) complexes with inequivalent metal centers. An investigation of the kinetics of peroxo formation was undertaken, using time-resolved UV−vis spectroscopy to determine the reaction order with respect to the diferrous precursor complex and O_2. Moreover, since X-ray structural studies revealed that the coordination number of one of the two iron atoms in the diiron(II) complexes could be modulated by intramolecular steric factors (vide supra), we were interested to determine whether such an effect might alter the kinetics of oxygenation.

Kinetics experiments were carried out at −77 °C on the pyridine adducts **6**, **7**, **13**, and **14**. Data were collected under pseudo-first-order conditions, with the diiron complex as the limiting reagent. Dioxygen concentrations were varied over a range of 3.1−15.4 mM. The time dependence of the buildup of the peroxo adduct was monitored at 600 nm (Figures 8A and S6−S8). The kinetic trace could be fit to first-order exponential curves for each complex. Plots of $\ln(k_\psi)$ vs $\ln[O_2]$ afforded straight lines with slopes near 1.0, indicating that the oxygenation reaction is first order in O_2 (Figures 8B and S6−S8). Second-order rate constants were obtained for the four iron complexes from the slopes derived from plots of k_ψ vs $[O_2]$ (Figures 8C and S6−S8). These rate constants are provided in Table 6 along with metrical data from the crystal structure determinations of **6**, **7**, and **13** describing the orientation of each bridging ancillary carboxylate. Activation parameters could not be obtained because the peroxo adducts decompose rapidly above −65 °C.

The first-order dependence in each reagent suggests that the rate-limiting step in these oxygenation reactions is a bimolecular collision between the diiron(II) complex and dioxygen. Within the series, the rate constants increase modestly, over a 4-fold range, with increasing steric demands of the carboxylate substituents. This kinetic trend correlates well with lengthening of the Fe2−O402 bond and decrease in τ as a function of the same steric parameters and may indicate that, in the transition state, cleavage of this bond is required to open a coordination site for O_2 binding to Fe2. This event corresponds to a rate-limiting carboxylate shift from monodentate bridging to *syn*,*syn*-bidentate bridging. Such structural/kinetic correlations must be viewed with caution, however, since the Mössbauer studies on the diiron(II) complexes reveal that the solid and solution structures may not be the same. Nevertheless, the trend does suggest that bond cleavage is involved in the rate determining step and argues against a mechanism where binding of the O_2 molecule to an iron center is impeded by the sterically encumbering carboxylate substituents. Such a mechanism was proposed for the oxygenation of a series of hydrotris(pyrazolyl)-borate iron(II) carboxylate complexes, where exceedingly bulky carboxylate substituents completely shut down the reaction.[41] By contrast, space-filling models of **6**−**16** reveal that the four- or five-coordinate iron center is unobstructed, irrespective of the carboxylate substituents (see Figure 4, for example).

The 1-alkylimidazole adducts **15** and **16** react to completion

(43) Clark, P. E.; Webb, J. *Biochemistry* **1981**, *20*, 4628.
(44) Dickson, D. P. E.; Berry, F. J. In *Mössbauer Spectroscopy*; Cambridge University Press: Cambridge, U.K., 1986.

Scheme 2

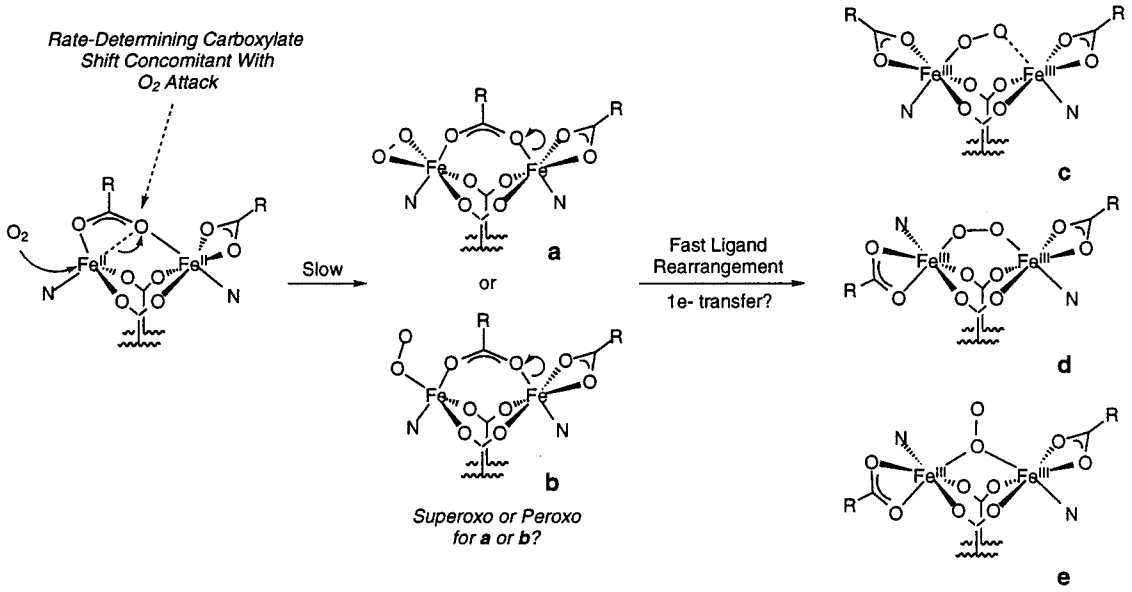

with O_2 within the time of mixing of the two reagents (<1 s), much more rapidly than the oxygenation rates observed for the pyridine complexes. Neither complex could be studied by the conventional methods employed here. The less sterically hindered analogue $[Fe_2(\mu\text{-PXDK})(\mu\text{-}O_2Ct\text{-Bu})(O_2Ct\text{-Bu})(\text{Me-Im})_2]$ was previously analyzed by stopped-flow UV−vis spectroscopy under very similar experimental conditions: $[Fe^{II}_2] = 0.8$ mM (after mixing) in THF, $T = -76$ °C, excess O_2,[23] revealing a pseudo-first-order rate constant of 300 s^{-1}. This value is more than a factor of 10^5 larger than the pseudo-first-order rate constants observed for the pyridine adducts. Such dramatically enhanced rates could be due in part to the minimal bonding interaction between the Fe2 and O402 in this complex. Because changes in this parameter have only a modest effect on the rate constants, however, we attribute most of the rate difference instead to the greater basicity of the 1-alkylimidazole ligand compared with pyridine. Such an electronic factor should lead to a significantly more negative midpoint potential for the $Fe^{III/II}$ couple with 1-alkylimidazole, thereby enhancing the thermodynamic driving force of the O_2 addition reaction and accelerating the rate.

(b) Proposed Mechanism for Peroxo Fomation. From these considerations we propose (Scheme 2) a working mechanism for the formation of the peroxo complex. Although peroxo buildup exhibits clean first-order dependence in each reaction component, the kinetics do not reveal whether the rate-limiting step leads directly to formation of the peroxo species. Very fast electron-transfer and/or ligand rearrangement steps may occur *after O_2 binding*, prior to final peroxo assembly. If formation of the peroxo complex occurs rapidly after the rate-limiting step, possibilities for the latter would be formation of a diiron(II)−O_2 adduct, an $Fe^{II}Fe^{III}$ superoxide complex, or isomerization of an intermediate complex. Two possibilities are represented by structures **a** and **b** in Scheme 2. For the final structure, the spectroscopic data are consistent with a bridged peroxo arrangement having inequivalent iron sites. To accommodate this feature, the mirror plane and rotational symmetry of the diiron-XDK framework must be eliminated. Structures **c**−**e** incorporate these properties through alterations in the orientation of the peroxide (**c**) or the other ligands (**d** and **e**). We consider these or closely related isomers to be viable candidates for the structures of the peroxo complexes presented here.

Comparison to Results on MMOH and RNR-R2. Several of the findings in the present modeling study are of potential relevance to chemistry that takes place at the carboxylate-bridged diiron active sites in MMOH and RNR-R2. Recent experiments reveal that the two enzymes can access common oxygen intermediates, the fate of which is exquisitely regulated according to their different oxidative functions. In one study, an RNR-R2 mutant (D84E) was prepared in which an aspartate residue in the active site was replaced with glutamate, affording an MMOH-like coordination environment.[45] With this modest change in the flexibility of a single carboxylate ligand, the D84E mutant remarkably afforded a diiron(III) peroxo intermediate that formed and decayed at rates comparable to those of H_{peroxo}. The product contained a stoichiometric quantity of a stable tyrosyl radical, most likely formed via intermediate X. These results lend credence to the assignment of the initial O_2 intermediate in native RNR-R2 as a diiron(III) peroxo species and reveal that the stability of peroxo intermediates in RNR-R2 and MMOH can be regulated by tuning the active-site ligands.

The interplay between the stereochemical demands of the carboxylate ligands, the extent of carboxylate shifting, and the ability to form a peroxo adduct illustrates one possible way in which the D84E mutant of RNR-R2 mutant might be able to access the diiron(III) peroxo intermediate not seen with the native protein.[45] The profound dependence of the rate of peroxodiiron(III) formation on the electronic properties of the N-donor ligand provides additional insight into how the protein cores might be tuned by the surrounding environment. The X-ray structure of MMOH revealed hydrogen bonding of the two histidine ligands coordinated to the dinuclear iron center (His147 and His246, Figure 1) to nearby aspartate residues in the four-helix bundle housing the active site of the enzyme.[46] Attenuation of this hydrogen bonding interaction, for example by the binding of protein B to the hydroxylase, could dramatically alter the rate of conversion of the diiron(II) form of the enzyme upon exposure to O_2, as observed in changing from pyridine to imidazole ligands in the present model studies. Further direct studies of the enzymes are required to test these

(45) Bollinger, J. M., Jr.; Krebs, C.; Vicol, A.; Chen, S.; Ley, B. A.; Edmondson, D. E.; Huynh, B. H. *J. Am. Chem. Soc.* **1998**, *120*, 1094.
(46) Rosenzweig, A. C.; Frederick, C. A.; Lippard, S. J.; Nordlund, P. *Nature* **1993**, *366*, 537.

suggestions. Several deficiencies in the models remain to be addressed by future work. Included are the fact that the H_{peroxo} intermediate has iron(III) centers that are indistinguishable by Mössbauer spectroscopy and that the present model complexes do not convert to a Q-type intermediate upon warming.[26] The restrictive "double-bridging" nature of the XDK ligand family may be responsible in part for the latter shortcoming and is currently being addressed.

Conclusions

A family of peroxo-bridged diiron(III) complexes has been prepared which matches exactly the combination of carboxylate and imidazole donors of the H_{peroxo} intermediate in the catalytic cycle of sMMO. A variety of methods, including UV−vis, EPR, resonance Raman, and Mössbauer spectroscopy, have been employed to elucidate their structures. The peroxo species have inequivalent iron coordination environments, a feature that is attributed either to an asymmetric peroxide bridge, a disproportionate arrangement of the ancillary carboxylate and nitrogen donor ligands about each iron center, or a combination of the two. Kinetic studies revealed the rate of peroxo formation to be first order in diiron(II) complex and O_2, implying a rate-determining bimolecular collision between reactants. The rate of peroxo formation varies inversely with the steric demands of the carboxylate substituents, implying that a carboxylate shift is associated with the rate-determining step. The oxygenation rate is affected much more dramatically by the basicity of the N-donor ligand, however, with a factor of $>10^5$ difference in the pseudo-first-order rate constants for 1-alkylimidazole versus pyridine ligation. These studies provide the most accurate compositional models of the H_{peroxo} intermediate reported to date, and their steric and electronic tunability have allowed us to address several of the many factors which affect their formation, structure, and stability.

Acknowledgment. This work was supported by a grant from the National Science Foundation and AKZO Corp. We thank Prof. W. M. Reiff (Northeastern University) for allowing us to use his Mössbauer spectrometer and A. M. Valentine and D. P. Steinhuebel for experimental assistance and many helpful discussions.

Supporting Information Available: Figures S1−S5, displaying fully labeled ORTEP diagrams for each reported structure, and Figures S6−S8, displaying kinetic data for the oxygenation of complexes **7**, **13**, and **14** (9 pages, print/PDF). X-ray crystallographic files, in CIF format, for complexes **6**, **7**, **12**, **13**, and **16**, are available on the Internet only. See any current masthead page for ordering information and Web access instructions.

JA981216S